Void Growth and Coalescence in Sigmoidal Hardening Porous Plastic Solids under Tensile and Shear Loading

Showren Datta
University of Houston
Shailendra Joshi
shailendra@uh.edu
University of Houston

Research Article

Keywords: First keyword, Second keyword, More

Posted Date: June 8th, 2023

DOI: https://doi.org/10.21203/rs.3.rs-3019594/v1

Additional Declarations: No competing interests reported.

Version of Record: A version of this preprint was published at International Journal of Fracture on April 5th, 2024. See the published version at https://doi.org/10.1007/s10704-024-00768-5.

Void Growth and Coalescence in Sigmoidal Hardening Porous Plastic Solids under Tensile and Shear Loading

Showren Datta · Shailendra P. Joshi

Received: date / Accepted: date

Abstract This work examines the void growth and coalescence in isotropic porous elastoplastic solids with sigmoidal material hardening via finite element three-dimensional unit cell calculations. The investigations are carried out for various combinations of stress triaxiality ratio ($\mathcal{T}$) and Lode parameter ($\mathcal{L}$) and considers a wide range of sigmoidal hardening behaviors with effective hardening rates spanning two decades. The effect of $\mathcal{L}$ is considered in the presence and in the absence of imposed shear stress. Our findings reveal that depending on the rate of sigmoidal hardening the cell stress-strain responses may exhibit two distinct transitions with respect to stress triaxiality $\mathcal{T}$. Further, the sigmoidal hardening rate also influences porosity evolution which may show stagnation before a runaway growth up to final failure. For a given $\mathcal{T}$-$\mathcal{L}$ combination, an imposed shear stress exacerbates the onset of coalescence relative to its counterpart with no imposed shear stress. We find that the *residual cell ductility* beyond the onset of coalescence is strongly influenced by the effective material hardening rate at high triaxiality levels.

Keywords First keyword · Second keyword · More

Mathematics Subject Classification (2020) MSC code1 · MSC code2 · more

1 Introduction

Strain hardening in elastoplastic materials has important consequences in ductile failure. In power-law hardening materials, the stress triaxiality ahead of a crack tip increases rapidly with the strain hardening exponent (n), which can have implications on material failure by cleavage or void growth [1]. On the other hand, higher values of n delay void growth under a constant stress state [2,3], thus creating a competitive scenario for ductile failure. While much work has been carried out to study void growth and coalescence in power-law hardening materials, the role of other material hardening characteristics has not been as well studied. Among those are materials exhibiting sigmoidal hardening, which is observed in some hexagonal close-packed metals (e.g., magnesium [4]), polymers [5], and even shape memory alloys [6]. Figure 1 shows illustrative sigmoidal stress-strain curves from polycrystal simulations of magnesium (Mg) alloys [7], which occurs because of profuse deformation twinning. While the underlying deformation mechanisms causing sigmoidal hardening may depend on the material, the broader stress-strain features include a two-stage hardening response characterized by an initial yield stress followed by an S-shaped curve culminating into a saturation-type behavior at large strains.

Showren Datta
Department of Mechanical Engineering
University of Houston

Shailendra P. Joshi
Department of Mechanical Engineering
University of Houston
Tel.: +1-713-743-6930
E-mail: shailendra@uh.edu

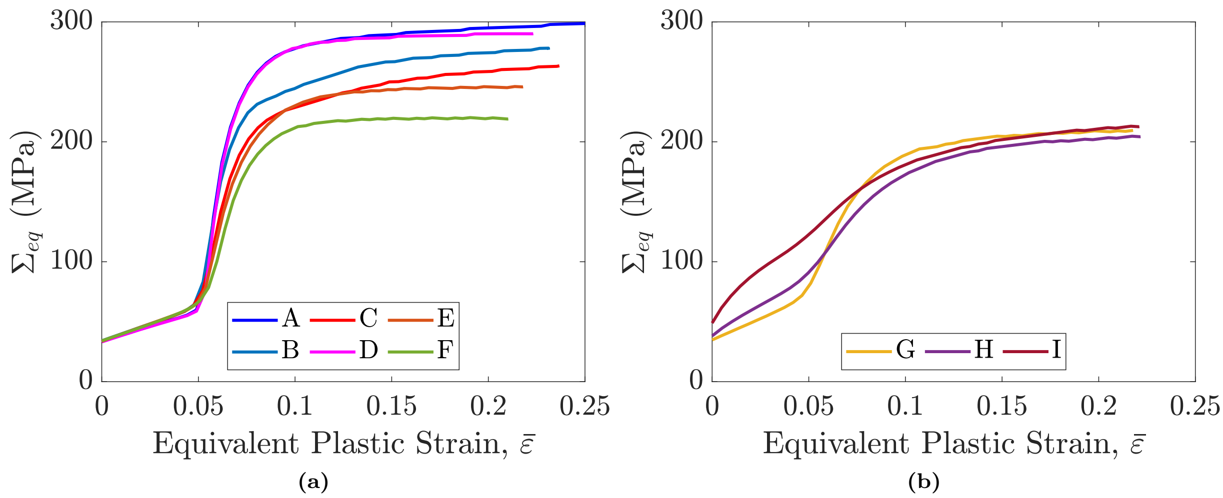

Fig. 1 Sigmoidal stress-strain responses of polycrystalline magnesium alloys with different initial textures (cases A-I). Panel (a) illustrates scenarios with similar hardening rates but different saturation stresses and (b) shows scenarios with similar saturation stress but different hardening rates. Data re-plotted from [7]

A recent work [8] investigated void growth and coalescence in isotropic porous elastoplastic solids showing sigmoidal material hardening. Those calculations were performed for axisymmetric tensile stress states characterized by a constant stress triaxiality ratio, $\mathcal{T} = \Sigma_{\mathrm{m}}/\Sigma_{\mathrm{eq}}$ where Σ_{m} and Σ_{eq} are respectively the mean normal stress and the equivalent stress. Thus, the salient observations did not account for the intermediate principal stress (Σ_2), which samples stress states between purely axisymmetric and shear-dominant. To consider the effect of Σ_2, the Lode parameter is introduced: $\mathcal{L} = (2\Sigma_2 - \Sigma_1 - \Sigma_3)/(\Sigma_1 - \Sigma_3)$ where $\Sigma_1 \geq \Sigma_2 \geq \Sigma_3$ are the principal stresses. The effect of $\mathcal{T}$, at fixed $\mathcal{L}$, on ductility (characterized by strain-to-failure, E_{c}) is well-known - an exponentially decreasing E_{c} with increasing $\mathcal{T}$. By way of contrast, the $E_{\mathrm{c}} - \mathcal{L}$ relationship at fixed $\mathcal{T}$ is not particularly well characterized even for conventional power-law hardening materials [9], let alone sigmoidally hardening materials. In power-law hardening materials, it appears that E_{c} is non-monotonic with $\mathcal{L}$ with the minimum occurring in the regime $-1.0 \lesssim \mathcal{L} \lesssim 0$ [10, 11, 12, 13], although there is equally compelling evidence of monotonically increasing E_{c} with increasing $\mathcal{L}$ [14, 15]. Recent micromechanical analysis [16] indicates that these trends are influenced by the initial porosity f_0 and $\mathcal{T}$. A more recent computational study reveals that imposed boundary conditions also play a crucial role in the way $E_c - \mathcal{L}$ relations manifest at fixed $\mathcal{T}$ [9].

With this background, we focus on three aspects pertaining to sigmoidal hardening materials. First, we investigate a wider and more realistic range of sigmoidal hardening parameters than those considered in Ref. [8]. Second, we assess the void growth and coalescence trends for these materials over a range of $\mathcal{T} - \mathcal{L}$ combinations. Third, we consider the $\mathcal{T} - \mathcal{L}$ combinations without ($\rho_{\mathrm{xy}} = 0$) and with ($\rho_{\mathrm{xy}} \neq 0$) an imposed shear stress.

2 Problem Formulation

In contrast to the axisymmetric finite element simulations in [8], we adopt a three-dimensional unit cell to model combined tensile and shear loading, Fig. 2. The computational setup comprises a cubic unit cell (initial dimension, L_0) with a spherical void (initial radius, R_0) at its center. Thus, the initial porosity is $f_0 = (4\pi R_0^3/3L_0^3)$. We define ligament parameters $\chi_{\mathrm{x}} = r_{\mathrm{x}}/L_{\mathrm{x}}$ and $\chi_{\mathrm{z}} = r_{\mathrm{z}}/L_{\mathrm{z}}$ where $r_i (i = \mathrm{x}, \mathrm{z})$ is the current void dimension in the i^{th} direction and L_i is the corresponding cell dimension. The unit cell is constrained by periodic kinematic boundary conditions. The unit cell faces are under traction via elastic springs connected to prescribed velocity boundary conditions to maintain a constant macroscopic triaxial stress state described by $\boldsymbol{\Sigma} = \Sigma_{\mathrm{xx}} e_{\mathrm{x}} \otimes e_{\mathrm{x}} + \Sigma_{\mathrm{yy}} e_{\mathrm{y}} \otimes e_{\mathrm{y}} + \Sigma_{\mathrm{zz}} e_{\mathrm{z}} \otimes e_{\mathrm{z}} + \Sigma_{\mathrm{xy}} e_{\mathrm{x}} \otimes e_{\mathrm{y}}$ in the lab frame (x,y,z). The macroscopic Cauchy stress components (Σ_{ij}) are volume-averaged quantities computed from the local (at each Gauss point) stress components (σ_{ij}) as $\Sigma_{\mathrm{ij}} = \dfrac{1}{V}\int_V \sigma_{\mathrm{ij}} dV$ where V is the current unit cell volume. Likewise, the volume-averaged macroscopic strains (E_{ij}) are $E_{\mathrm{ij}} = \dfrac{1}{V}\int_V e_{\mathrm{ij}} dV$ where e_{ij} is a logarithmic strain component at each Gauss point. The macroscopic mean stress is $\Sigma_{\mathrm{m}} = (1/3)\mathrm{tr}\,\boldsymbol{\Sigma}$ and the macrosopic equivalent stress is $\Sigma_{\mathrm{eq}} = \sqrt{(3/2)\boldsymbol{\Sigma}' : \boldsymbol{\Sigma}'}$. Likewise, the macroscopic effective strain is $E_{\mathrm{eq}} = \sqrt{(2/3)\mathbf{E}' : \mathbf{E}'}$.

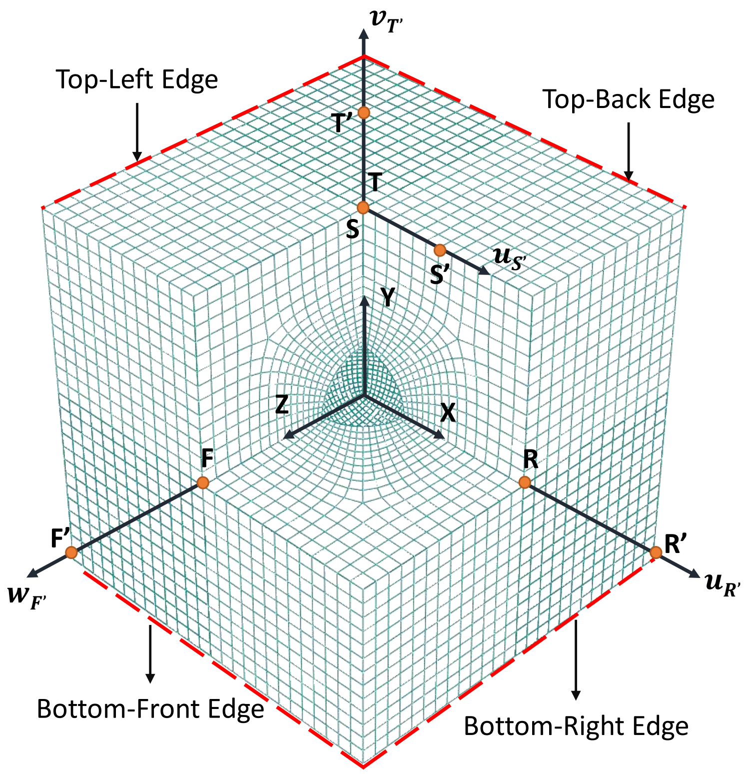

Fig. 2 The finite element unit cell with an initial void volume fraction of 0.01. The model contains $\sim 28,850$ linear brick elements (C3D8 in ABAQUS).

Here, given a second-order tensor $\mathbf{A}$, we write its deviatoric part as $\mathbf{A}' = \mathbf{A} : \mathbb{J}$ with $\mathbb{J} = \mathbb{I} - (1/3)\mathbf{I} \otimes \mathbf{I}$ with $\mathbb{I}$ and $\mathbf{I}$ being the fourth-order and second-order identity tensors, respectively.

With the y-axis as the primary tensile loading direction, the stress triaxiality ($\mathcal{T}$) and Lode parameter ($\mathcal{L}$) are given by [17]:

$$\mathcal{T} = \frac{\sqrt{2}(1 + \rho_{\mathrm{xx}} + \rho_{\mathrm{zz}})}{3\sqrt{(1-\rho_{\mathrm{xx}})^2 + (1-\rho_{\mathrm{zz}})^2 + (\rho_{\mathrm{xx}} - \rho_{\mathrm{zz}})^2 + 6\rho_{\mathrm{xy}}^2}}\ \mathrm{sign}(\varSigma_{\mathrm{yy}}) \tag{1a}$$

$$\mathcal{L} = -\frac{(1 + \rho_{\mathrm{xx}} - 2\rho_{\mathrm{zz}})}{\sqrt{(1-\rho_{\mathrm{xx}})^2 + 4\rho_{\mathrm{xy}}^2}}\ \mathrm{sign}(\varSigma_{\mathrm{yy}}); \tag{1b}$$

where $\rho_{\mathrm{xx}} = \varSigma_{\mathrm{xx}}/\varSigma_{\mathrm{yy}}$, $\rho_{\mathrm{zz}} = \varSigma_{\mathrm{zz}}/\varSigma_{\mathrm{yy}}$, and $\rho_{\mathrm{xy}} = \varSigma_{\mathrm{xy}}/\varSigma_{\mathrm{yy}}$ are the stress ratios.

Fig. 3 shows the uniaxial material hardening curves considered in the present study. These hardening behaviors are described by the Boltzmann function, which mimics the sigmoidal behaviors (e.g., Fig. 1):

$$\bar{\sigma} = \sigma_f + \frac{\sigma_i - \sigma_f}{1 + \exp(k)} \quad ; \quad k = \frac{\bar{\varepsilon} - n\varepsilon_0}{\mathrm{d}\varepsilon} \tag{2}$$

where $\bar{\sigma}$ and $\bar{\varepsilon}$ are respectively the equivalent stress and equivalent plastic strain. In Eq. 2, σ_i is the lower saturation stress, σ_f the upper saturation stress, $\varepsilon_0 \equiv (1/2)(\varepsilon_i + \varepsilon_f)$ and $\mathrm{d}\varepsilon \equiv (1/4)(\varepsilon_f - \varepsilon_i)$ with ε_i and ε_f being the strains corresponding to σ_i and σ_f, respectively. The factor n (set equal to 1.75) ensures that the $(\bar{\sigma})_{\mathrm{yield}} \equiv \sigma_i$ for the range of material investigated here.

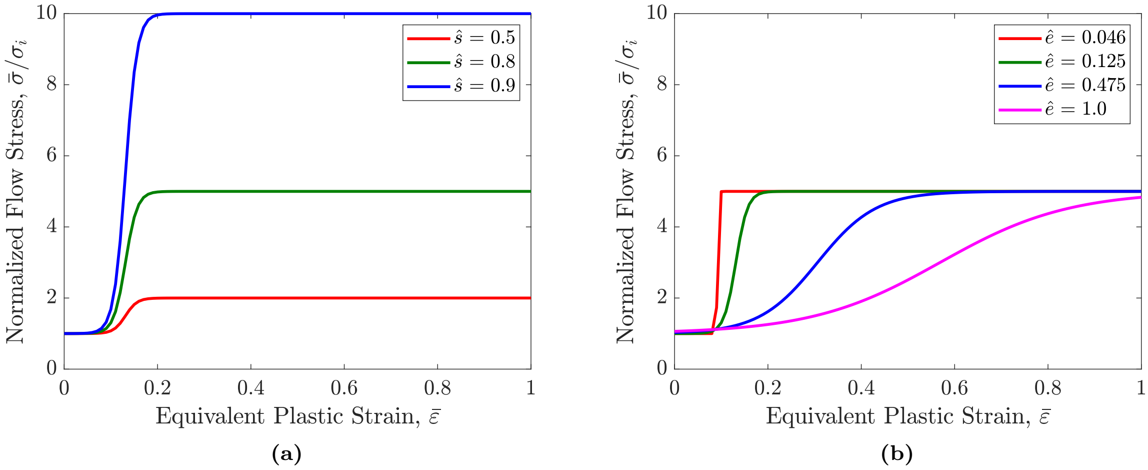

Fig. 3 Different sigmoidal hardening scenarios considered in this work: (a) Constant $\hat{s}$, varying ε_f, and (b) Constant $\hat{e}$, varying σ_f.

Using Eq. 2, we define a non-dimensional parameter $\hat{h} = \hat{s}/\hat{e}$ indicating an *effective* material hardening rate where $\hat{s} = (\sigma_f - \sigma_i)/\sigma_f$ and $\hat{e} = (n\varepsilon_f - \varepsilon_i)$. In this work, we consider $\hat{s} \in \{0.5, 0.8, 0.9\}$ and $\hat{e} \in \{0.046, 0.125, 0.475, 1.0\}$, which samples a wide range of material hardening rates $0.5 \lesssim \hat{h} \lesssim 20$. Very roughly, $\hat{e} = 0.046$ would resemble a material with Voce-type hardening while $\hat{e} = 1.0$ would mimic a power-law hardening material, cf. Fig. 3b. Of course, these semblances will depend on $(\sigma_f - \sigma_i)$. For discussion purposes, we refer to $\hat{e} \in \{0.046, 0.125\}$ as *rapid hardening* (RH), $\hat{e} = 0.475$ as *intermediate hardening* (IH), and $\hat{e} = 1.0$ as *slow hardening* (SH) materials. For all the cases, we set $\sigma_i = 10$ MPa and $\varepsilon_i = 0.05$. The material is assumed to be elastically isotropic with Young's modulus $E = 210$ GPa and Poisson's ratio $\nu = 0.3$.

3 Results

In what follows, we discuss illustrative results that highlight key trends for $0.75 \leq \mathcal{T} \leq 3.0$ and $-1.0 \leq \mathcal{L} \leq 1.0$. The bounds for $\mathcal{T}$ characterize stress states ranging in specimens with blunt notches ahead to those ahead of crack tips and those for $\mathcal{L}$ range from generalized tension ($\mathcal{L} = -1.0$) to generalized shear ($\mathcal{L} = 0$), and generalized compression ($\mathcal{L} = 1.0$). The results for porous unit cells under uniaxial tension ($\mathcal{T} = 1/3$) are not included for brevity as they are indistinguishable from their pristine counterparts.

To identify the onset of coalescence, we adopt the strain-based criterion [18], which identifies coalescence onset as the critical equivalent strain, E_c, at which the cell straining transitions from a triaxial to uniaxial mode. Further, we define failure strain, E_f, as the equivalent strain at which one or both the ligament parameters χ_i reach a critical value χ_f. In theory, failure occurs when $\chi = 1$, however from a numerical standpoint we set $\chi_f = 0.95$. In situations where E_f occurs before E_c, we take $E_c = E_f$.

3.1 Macroscopic responses in the absence of applied shear stress

For brevity, we present the results for $\hat{s} = \{0.5, 0.8\}$ and $\hat{e} = \{0.046, 0.125, 0.475, 1.0\}$ for a range of $\mathcal{T}$-$\mathcal{L}$ combinations. Fig. 1 summarizes the stress ratios for the $\mathcal{T}$-$\mathcal{L}$ combinations keeping $\rho_{\mathrm{xy}} = 0$. Fig. 4 shows the cell responses of materials with $\hat{s} = 0.5$ but varying $\hat{e}$ values. The results for $\mathcal{L} = 1$ are not shown here to avoid overcrowding as the strains accumulated in those cases are much larger and rapid failure may not occur. At a fixed $\mathcal{T}$, $\mathcal{L} = -1$ presents the most severe scenario insofar as the porosity evolution is concerned, which in turn governs stress softening and hence, E_c. Beyond this expected trend at this level of f_0 [16], sigmoidal hardening produces a rich suite of responses that intimately depend on $\mathcal{T}$ and whose qualitative features are persistent across the range of $\mathcal{L}$.

Table 1 Stress ratios for $\mathcal{T}$-$\mathcal{L}$ combination for tensile loading.

	$\mathcal{L}=-1.0$		$\mathcal{L}=-0.5$		$\mathcal{L}=0.0$		$\mathcal{L}=0.5$		$\mathcal{L}=1.0$	
	$\rho_{\rm xx}$	$\rho_{\rm zz}$	$\rho_{\rm xx}$	$\rho_{\rm zz}$	$\rho_{\rm xx}$	$\rho_{\rm zz}$	$\rho_{\rm xx}$	$\rho_{\rm zz}$	$\rho_{\rm xx}$	$\rho_{\rm zz}$
$\mathcal{T}=0.75$	0.29	0.29	0.21	0.41	0.13	0.57	0.085	0.77	0.077	1.00
$\mathcal{T}=1.0$	0.40	0.40	0.33	0.50	0.27	0.63	0.24	0.81	0.25	1.00
$\mathcal{T}=2.0$	0.63	0.63	0.58	0.69	0.55	0.78	0.55	0.89	0.57	1.00
$\mathcal{T}=3.0$	0.73	0.73	0.70	0.77	0.68	0.84	0.68	0.92	0.70	1.00

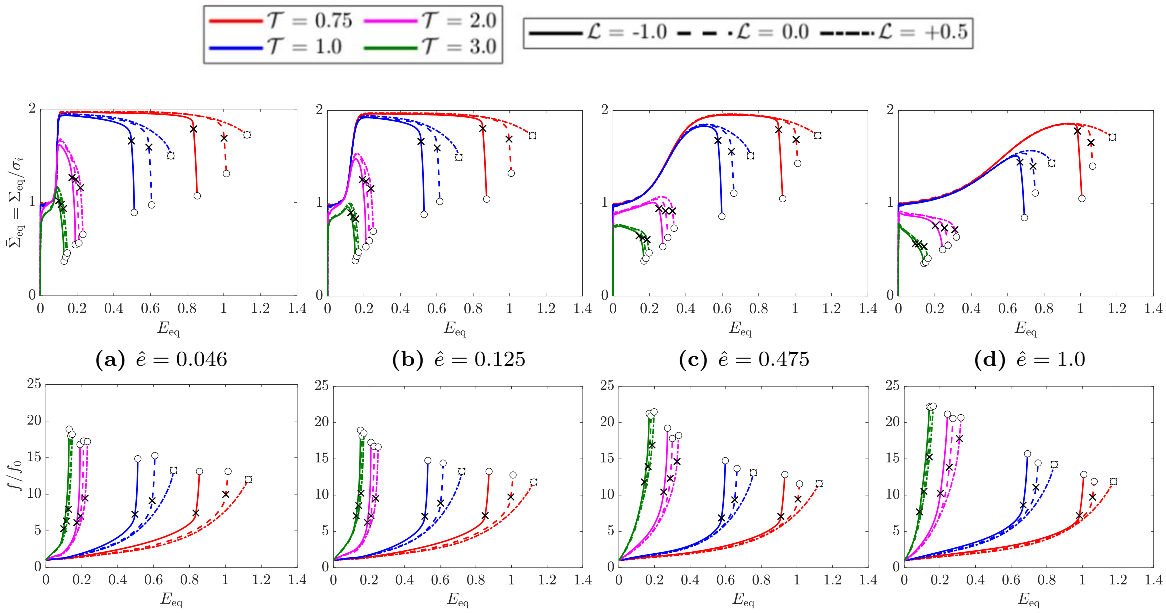

(a) $\hat{e}=0.046$ **(b)** $\hat{e}=0.125$ **(c)** $\hat{e}=0.475$ **(d)** $\hat{e}=1.0$

(e) $\hat{e}=0.046$ **(f)** $\hat{e}=0.125$ **(g)** $\hat{e}=0.475$ **(h)** $\hat{e}=1.0$

Fig. 4 For $\rho_{\rm xy}=0$, effects of $\mathcal{T},\mathcal{L}$, and $\hat{e}$ on (a-d) normalized equivalent stress-strain responses and (e-h) normalized porosity (f/f_0) evolution for $\hat{s}=0.5$. The "×" represents E_c and "∘" represents E_f.

Consider RH materials first (Fig. 4a and 4b). Under moderate $\mathcal{T}$ levels ($\lesssim 1.0$) the strain ($E_{\rm peak}$) corresponding to the peak stress is approximately equal to the material saturation strain (ε_f), i.e., $E_{\rm peak}\approx\varepsilon_f$. By way of comparison, E_c, (marked by ×) is much larger, i.e., $E_c \gg E_{\rm peak}$. With increasing $\mathcal{L}$ the gap between $E_{\rm peak}$ and E_c increases at these $\mathcal{T}$ levels. At higher $\mathcal{T}$ levels the effect of $\mathcal{L}$ is diminished such that at $\mathcal{T}=3.0$, $E_c\approx E_{\rm peak}$.

In IH materials (Fig. 4c) the gap between $E_{\rm peak}$ and E_c is smaller compared to RH materials at $\mathcal{T}\lesssim 1.0$. Interestingly, at $\mathcal{T}=2.0$ the cell responses exhibit strain hardening leading up to the coalescence onset; i.e., $E_c\approx E_{\rm peak}$. In contrast, at $\mathcal{T}=3.0$ gradual stress softening occurs immediately following the initial yield with no evidence of sigmoidal hardening and $E_c\gg E_{\rm peak}$.

In SH materials (Fig. 4d), $E_c\approx E_{\rm peak}$ for $\mathcal{T}\lesssim 1.0$ with a strain hardening response leading up to the coalescence onset. For $\mathcal{T}\gtrsim 2.0$ the responses are qualitatively similar to those of IH materials at $\mathcal{T}=3.0$ together with $E_c\gg E_{\rm peak}$.

The porosity evolution in RH, IH, and SH materials (Fig. 4e-4h) is largely insensitive to $\mathcal{L}$ up to $E_{\rm peak}$. Beyond that, it shows sensitivity to $\mathcal{L}$ for $\mathcal{T}\lesssim 2.0$. Note that, at a given $\mathcal{L}$ the critical porosity (f_c) at E_c is relatively insensitive to $\hat{e}$ at moderate triaxiality levels ($\mathcal{T}\lesssim 1.0$) but depends strongly on $\mathcal{T}$ at higher $\mathcal{T}$ levels.

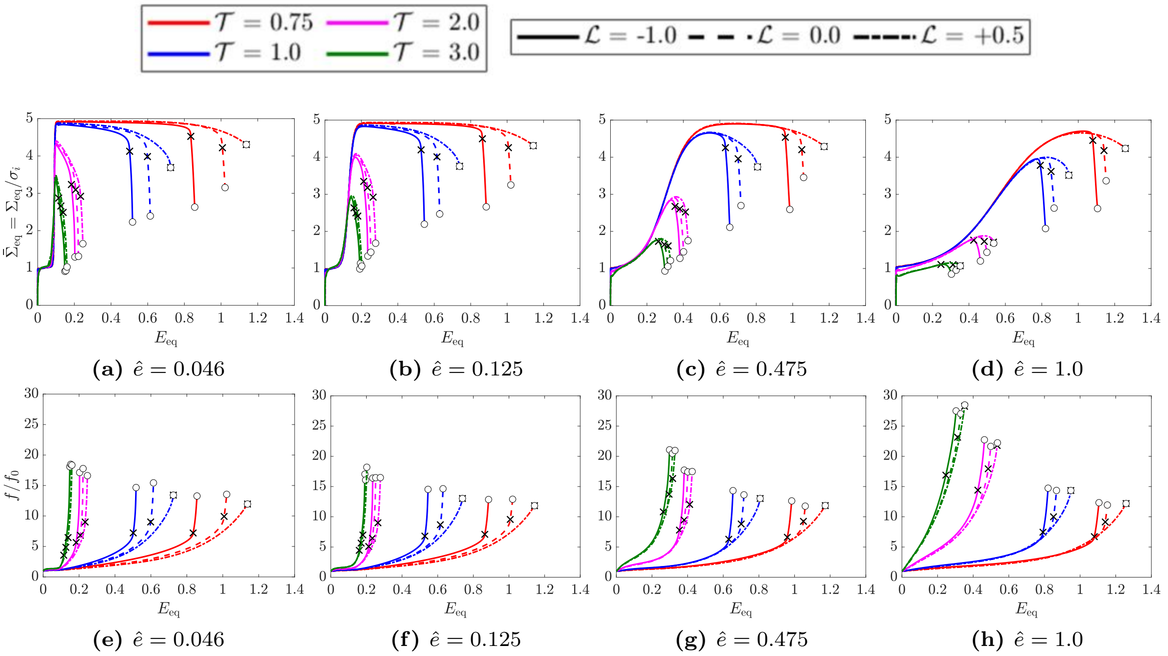

Fig. 5 For $\rho_{\mathrm{xy}} = 0$, effects of $\mathcal{T}, \mathcal{L}$, and $\hat{e}$ on (a-d) normalized equivalent stress-strain responses and (e-h) normalized porosity (f/f_0) evolution for $\hat{s} = 0.5$. The "×" represents E_c and "○" represents E_f.

Fig. 5 collates the results for $\hat{s} = 0.8$. While the broad trends are similar to those seen in $\hat{s} = 0.5$ at $\mathcal{T} \leq 1.0$, important differences can be spotted at higher $\mathcal{T}$ levels. Unlike $\hat{s} = 0.5$, only one transition is seen as a function of $\mathcal{T}$. For a given $\hat{e}$, the cell response transitions from $E_c \gg E_{\mathrm{peak}}$ at moderate $\mathcal{T}$ levels ($\mathcal{T} \lesssim 1.0$) to a response characterized by $E_c \approx E_{\mathrm{peak}}$ at high $\mathcal{T}$ levels $\gtrsim 2.0$. Moreover, at $\mathcal{T} \gtrsim 2.0$ the initial yield continues to occur at σ_i (i.e., $\bar{\Sigma}_{\mathrm{eq}} = 1$) unlike in the case of $\hat{s} = 0.5$ where $\bar{\Sigma}_{\mathrm{eq}} < 1$.

In Fig. 5e-5h, the porosity appears to follow an exponential evolution. However, a closer look (Fig. 6) reveals that porosity initially begins to increase, then stagnates (or slows down) over an extended strain range, and then increases rapidly again, see RH responses Fig. 6a and 6b. [8] observed similar responses in RH materials for $\mathcal{L} = -1.0$ and found that they occurred due to large differences in the magnitude of the flow stresses between the polar and the equatorial regions of the void as a result of the sigmoidal material hardening. What is interesting to note here is that it prevails over a much wider range of $\hat{s}$ and $\hat{e}$ values (Fig. 6c) and over a broader range of $\mathcal{T}$ across the entire range of $\mathcal{L}$. In comparison, the stagnation tendency is much less in SH materials (Fig. 5h).

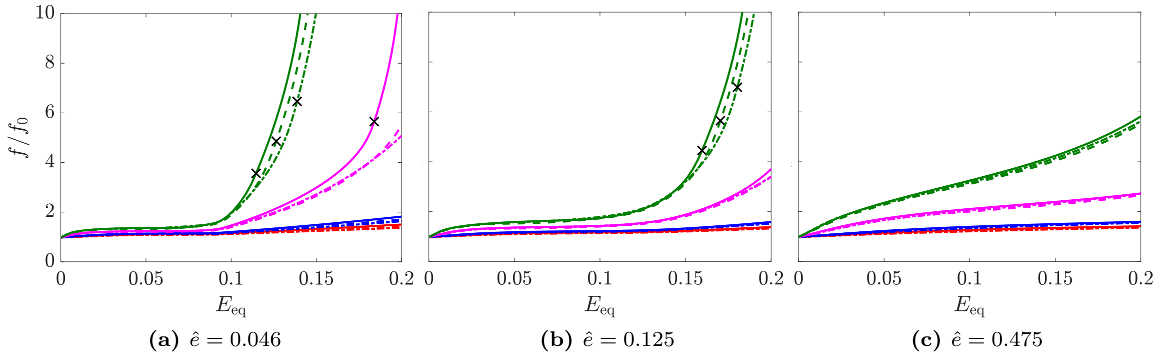

Fig. 6 Early stages of porosity evolution for $\hat{s} = 0.8$, $\rho_{\mathrm{xy}} = 0$.

Fig. 7 illustrates the evolution of the ligament parameters (χ_{x} and χ_{z}) for $\hat{s} = 0.8$. Note that χ is indicative of ligament thinning between adjacent voids. As expected, at $\mathcal{L} = -1.0$ the lateral void growth is symmetric ($\chi_{\mathrm{x}} = \chi_{\mathrm{z}}$) irrespective of $\mathcal{T}$. For $\mathcal{L} = 0$, initially $\chi_{\mathrm{z}} > \chi_{\mathrm{x}}$ but with progressive deformation χ_{x} increases rapidly and overtakes χ_{z}. This occurs because, while $r_{\mathrm{x}} < r_{\mathrm{z}}$ at all times, with deformation

$L_x \ll L_z$ owing to the Poisson's effect combined with $\rho_{xx} \ll \rho_{zz}$. As seen in Fig. 7b, all combinations of $\mathcal{T}$ and $\hat{e}$ show this behavior but the effect is most discernible for $\mathcal{T} = 1$ and $\hat{e} = 1.0$. In such scenarios, E_f occurs when $\chi_x = \chi_f$. Another notable characteristic evident in RH materials is that, for both values of $\mathcal{L}$ the χ evolution is markedly slowed down in the regime between the initial yield and the second stage hardening. It coincides with the slowing down of the porosity evolution, cf. Fig. 6. This behavior is similar to the evolution of χ isotropic cases at $\mathcal{L} = -1.0$ [8].

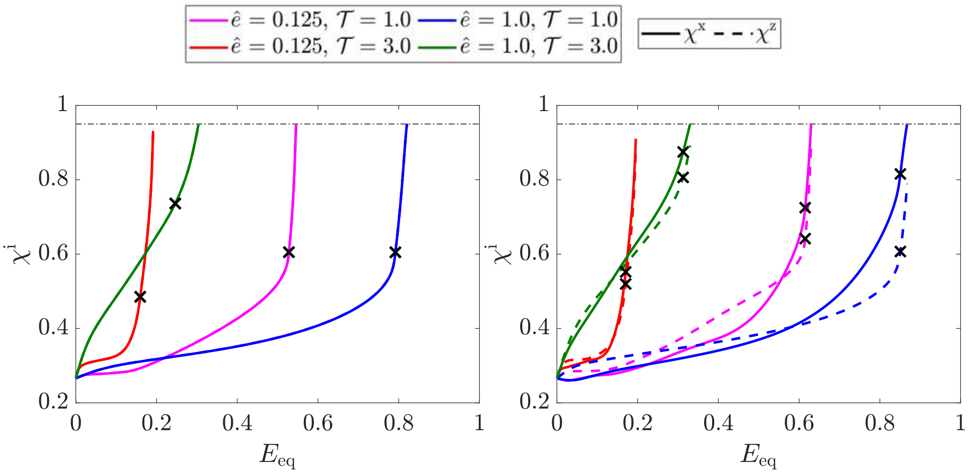

(a) $\mathcal{L} = -1.0$ **(b)** $\mathcal{L} = 0.0$

Fig. 7 Effect of $\hat{e}$ and $\mathcal{T}$ ligament parameter (χ^i) evolution at (a) $\mathcal{L} = -1.0$ and (b) $\mathcal{L} = 0$. $\hat{s} = 0.8$, $\rho_{xy} = 0$. $\times$ indicates value at E_c and the dashed horizontal line indicates χ_f.

We note in passing that $\hat{s} = 0.9$ shows similar characteristics as $\hat{s} = 0.8$.

Fig. 8a-8c shows the effect of the Lode parameter on E_c for the RH, IH, and SH material types with varying $\hat{s}$ values at different $\mathcal{T}$ levels. Results corresponding to $\mathcal{L} = 1.0$ are not included as in all the cases, E_c is attained when $\chi = \chi_{crit}$, which occurs at very large values of E_{eq}. As seen, $\mathcal{L}$ plays a role in E_c at $\mathcal{T} = 0.75$ and $\mathcal{T} = 1.0$ in RH (Fig. 8a) and IH (Fig. 8b) materials. In fact, the range of E_c for $-1.0 \le \mathcal{L} \le +0.5$ is the same for RH and IH materials. In contrast, E_c of SH materials is much less sensitive to $\mathcal{L}$, particularly at $\mathcal{T} \ge 1.0$ but increases with increasing $\hat{s}$, Fig. 8c. For a fixed $\mathcal{T} - \mathcal{L}$ combination, a higher $\hat{s}$ (at a fixed $\hat{e}$) results in higher E_c. Fig. 8d-8i capture the ligament parameter values corresponding to E_c. For any $\mathcal{T}$, $\mathcal{L} = -1.0$ gives $\chi_c^x = \chi_c^z$, as expected. Interestingly, while χ_c^x increases with increasing $\mathcal{L}$, the changes in χ_c^z are relatively modest (Fig. 8g-8i). As a result, for $\mathcal{L} > -1.0$, $\chi_c^x > \chi_c^z$ despite the fact that $\rho_{zz} > \rho_{xx}$. As can be seen, this trend prevails over the range of material parameters $(\hat{s}, \hat{e})$ and triaxiality levels considered here.

3.2 Macroscopic responses in the presence of applied shear stress

In this section, we present illustrative results with $\rho_{xy} \neq 0$ for $\hat{s} = 0.8$ for varying $\hat{e}$ and compare them against the corresponding cases with $\rho_{xy} = 0$. Fig. 2 summarizes the applied stress ratios for particular $\mathcal{T}$-$\mathcal{L}$ combinations. In the present work, we adopt the stress ratios such that $\Sigma_{yy} \ge \{\Sigma_{xx}, \Sigma_{zz}\}$. Note that the angle ϕ between the primary loading direction and the direction of the maximum principal stress varies for each case, which is different from the problem of constant ϕ considered by [11] and [13] but similar to the work of [17].

Table 2 Stress ratios for $\mathcal{T}$-$\mathcal{L}$ combination for combined tension and shear loading. ϕ denotes the angle between the loading axis and the maximum principal stress direction.

	$\mathcal{L} = -1.0$				$\mathcal{L} = -0.5$				$\mathcal{L} = 0.0$				$\mathcal{L} = 0.5$				$\mathcal{L} = 1.0$			
	ρ_{xx}	ρ_{zz}	ρ_{xy}	ϕ	ρ_{xx}	ρ_{zz}	ρ_{xy}	ϕ	ρ_{xx}	ρ_{zz}	ρ_{xy}	ϕ	ρ_{xx}	ρ_{zz}	ρ_{xy}	ϕ	ρ_{xx}	ρ_{zz}	ρ_{xy}	ϕ
$\mathcal{T} = 0.75$	0.5	0.34	0.33	26.2	0.35	0.45	0.30	21.5	0.25	0.63	-0.30	19.4	0.15	0.82	-0.23	14.4	0.08	1.0	-0.05	3.2
$\mathcal{T} = 2.0$	0.7	0.65	-0.13	20.1	0.7	0.74	-0.17	24.1	0.59	0.80	-0.10	13.4	0.60	0.92	-0.12	15.4	0.58	1.0	0.03	4.2

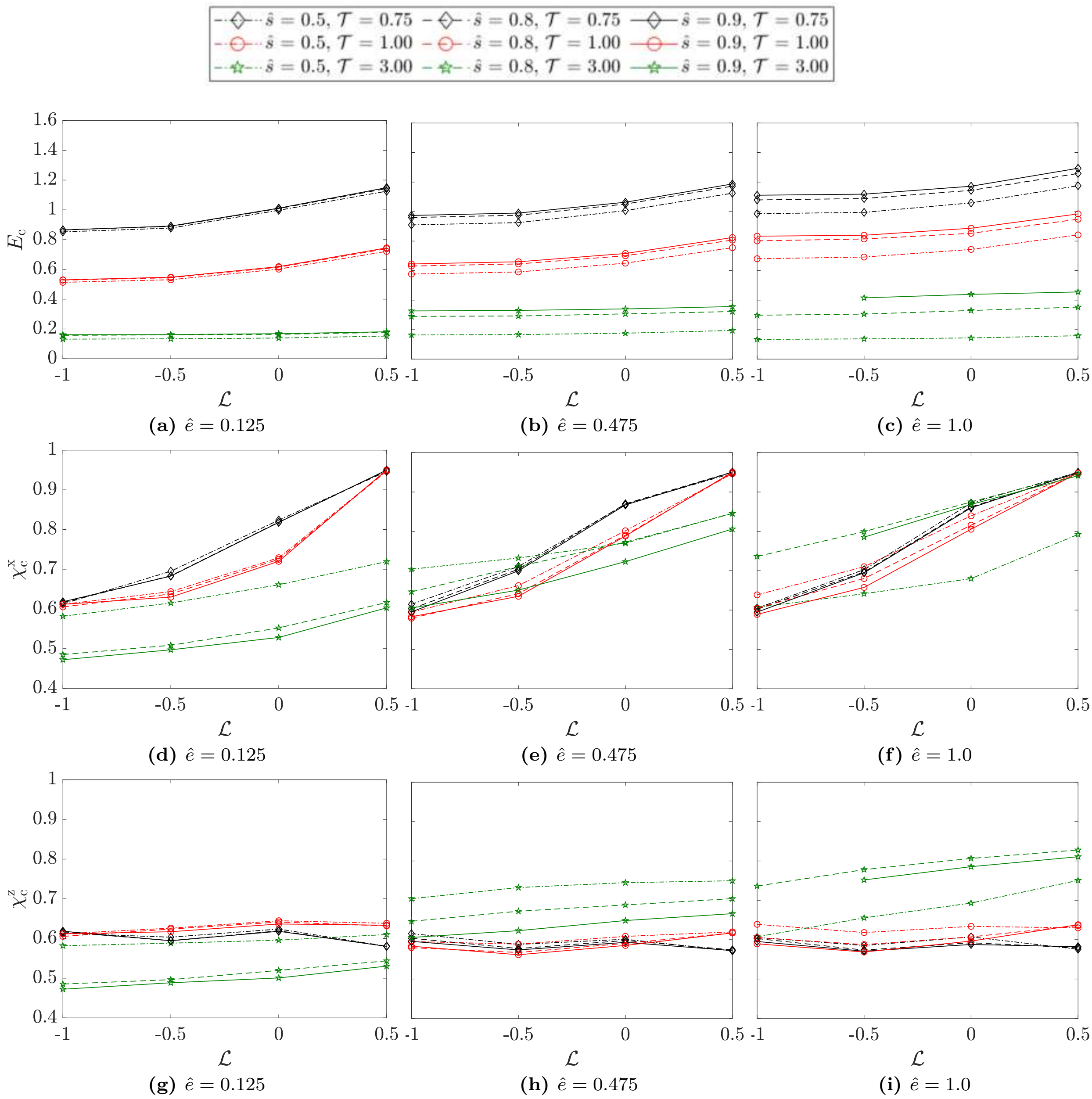

Fig. 8 Effects of $\mathcal{T}$, $\mathcal{L}$, and $\hat{s}$ on (a-d) E_c, (e-h) χ_c^x, and (g-i) χ_c^z for varying $\hat{e}$. $\rho_{xy} = 0$.

Fig. 9a, 9c, and 9e collate the cell responses at $\mathcal{T} = 0.75$ for RH ($\hat{e} = 0.125$), IH ($\hat{e} = 0.475$), and SH ($\hat{e} = 1.0$) materials. Note that the peak stress in RH and SH materials is nearly the same as the peak stress for the pristine matrix material. In comparison, the SH material exhibits lower peak stress, an effect of the rate of sigmoidal hardening dictated solely by $\hat{e}$ (as $\hat{s}$ is constant) and is agnostic to ρ_{xy}. While the broad trends for $\rho_{xy} \neq 0$ are similar to $\rho_{xy} = 0$, some important differences are seen. For all three material types, ρ_{xy} has no effect on the cell responses at $\mathcal{L} = 1.0$. With decreasing $\mathcal{L}$, however, imposing shear stress expedites the rapid porosity evolution and hence, lowers E_c.

At $\mathcal{T} = 2.0$ (Fig. 9b, 9d, and 9f) the same materials exhibit different qualitative features compared to $\mathcal{T} = 0.75$, particularly for $\mathcal{L} \in \{-1.0, 0.0\}$. For the RH (Fig. 9b) and IH (Fig. 9d) materials, the difference in E_c without and with shear stress is practically indistinguishable. Notwithstanding this, beyond the onset of coalescence, the stress softening and porosity evolution show a more gradual evolution in the presence of shear stress. The slower porosity evolution could result in a delayed final failure thereby improving the overall material resistance. In comparison, the SH material (Fig. 9f) shows a somewhat higher E_c for $\rho_{xy} \neq 0$ than for $\rho_{xy} = 0$ in contrast to the lower triaxiality case (cf. Fig. 9e). These differences in E_c can be important at such high $\mathcal{T}$ levels.

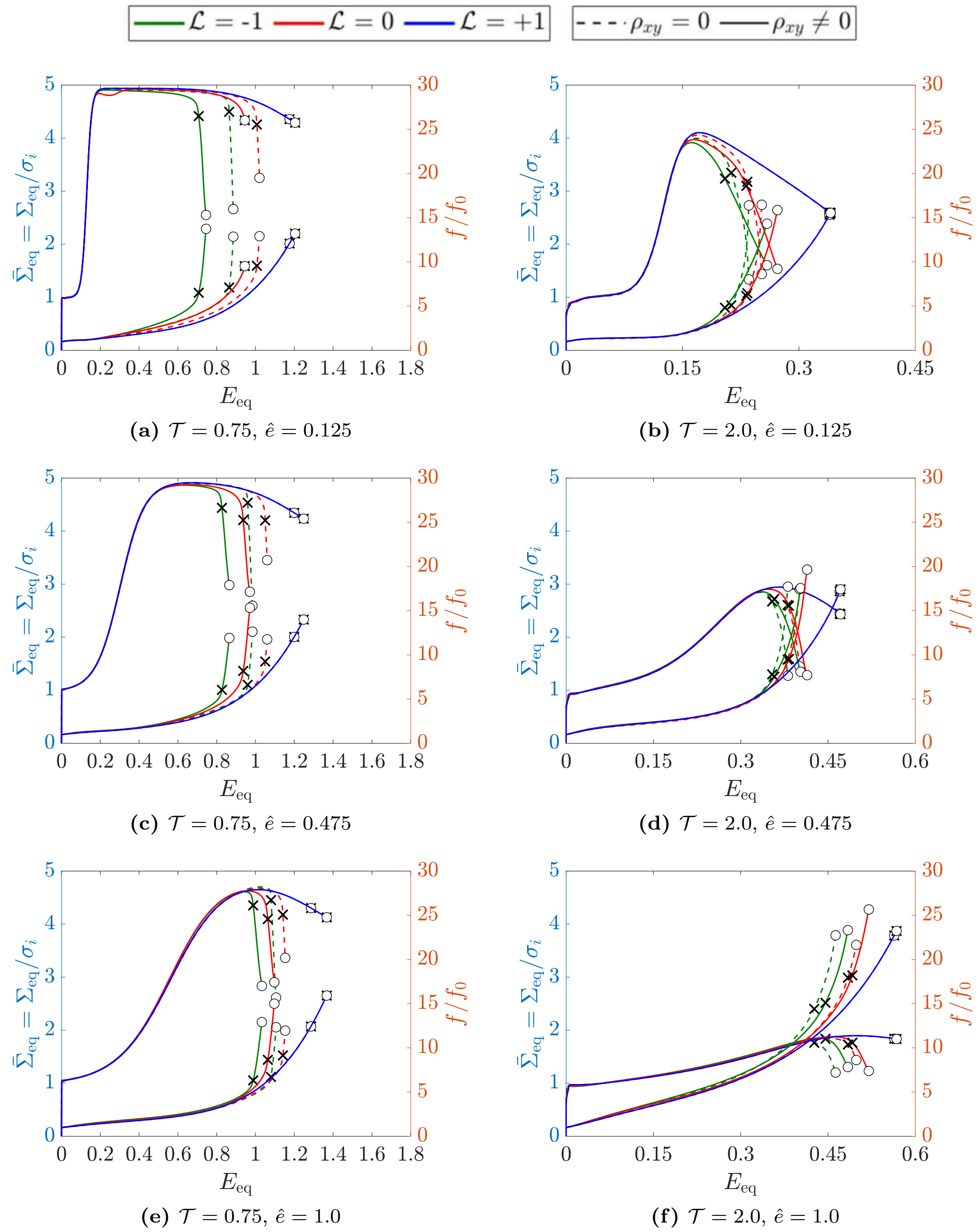

Fig. 9 Effect of imposed shear stress (solid lines) on macroscopic cell responses under prescribed $\mathcal{T} - \mathcal{L}$ combinations in (a-b) RH, (c-d) IH, and (e-f) SH materials. Dashed lines are the corresponding results with $\rho_{\text{xy}} = 0$. The results are shown for $\hat{s} = 0.8$.

The overall trends of E_c and χ_c^i, are similar to those in Fig. 8 and are discussed in the context of sigmoidal material parameters in the next section.

4 Discussion

In the preceding section, we consider the Lode parameter effect on the porous response of sigmoidally hardening materials in the absence or presence of imposed shear stress. In the latter case, the angle ϕ made by the loading axis with the major principal stress direction comes into play (cf. Fig. 2). Generally (but not always), a fixed value of ϕ is chosen such that E_c is minimized for a particular $\mathcal{T}$-$\mathcal{L}$ combination [11] and is obtained by trial and error [13]. Here, we have not performed such a study.

Another aspect pertains to material ductility. In theory, ductility (failure strain) is the strain at which stress drops to zero, which coincides with vanishing inter-void ligament, i.e., $\chi = 1$. As alluded to earlier, E_c

indicates the strain at which the process of coalescence initiates and is often adopted as a ductility criterion. A recent computational study [9] shows that the trends of ductility with $\mathcal{L}$ can significantly vary depending on the choice of ductility criterion and unit cell boundary conditions, and therefore, material ductility is open to interpretation. This is in addition to the dependence of ductility on the initial porosity [16,19]. Recently, Benzerga and colleagues [20,21,22,19] have introduced the concept of *unhomogeneous* yielding (UY). For axisymmetric stress states, the strain corresponding to UY is identical to E_c. On the other hand, for stress states that deviate from axisymmetry, the strain associated with the first occurrence of UY may be different from E_c. While UY onset appears to be a useful indicator, an unambiguous representation of ductility under general proportional loading states seems to be an open question.

With these caveats, we discuss material failure trends from the viewpoint of material hardening ($\hat{s}$ and $\hat{e}$).

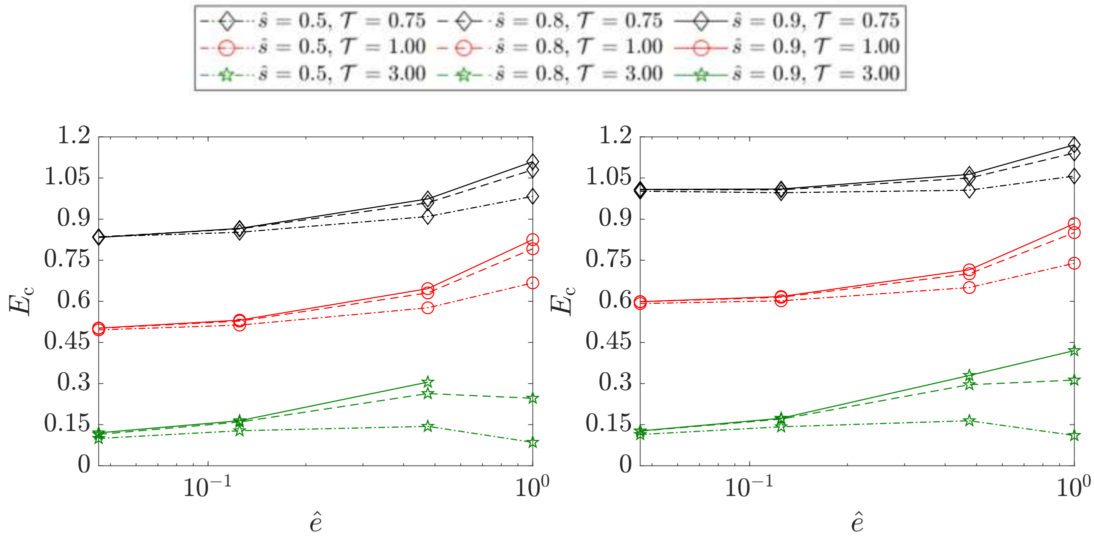

(a) $\mathcal{L} = -1.0$ **(b)** $\mathcal{L} = 0$

Fig. 10 Effect of $\hat{e}$ on the strain to coalescence (E_c) for illustrative cases of $\mathcal{L}$. $\rho_{\mathrm{xy}} = 0$

Fig. 10 collates the combined role of loading and material parameters on E_c for $\rho_{\mathrm{xy}} = 0$. Details aside, these results indicate that E_c depends on the *nature* of sigmoidal hardening rather than the effective sigmoidal hardening rate $\hat{h} = \hat{s}/\hat{e}$. In other words, $\hat{h}$ does not serve as a unique descriptor of the sigmoidal material hardening. That is, two materials with different $\{\hat{s}, \hat{e}\}$ combinations giving the same $\hat{h}$ will not give the same E_c. The calculations suggest that in such a scenario, a material with higher $\hat{e}$ and $\hat{s}$ values tends to show better ductility than its counterpart with a lower $\hat{e}$ and $\hat{s}$ values.

Fig. 11 illustrates how $\hat{e}$ affect E_c for $\hat{s} = 0.8$. When $\rho_{\mathrm{xy}} = 0$, E_c increases with $\hat{e}$ for $\mathcal{T} = 0.75$ (and $\mathcal{T} = 1.0$, not shown). While not shown here, at $\mathcal{T} = 3.0$ the trend of E_c depends on $\hat{s}$. For $\hat{s} = 0.5$, E_c is insensitive to $\hat{e}$ while for $\hat{s} = 0.9$ E_c increases with $\hat{e}$. The case of $\hat{s} = 0.8$ demonstrates an intermediate trend in that E_c increases with $\hat{e}$ but saturates beyond $\hat{e} \sim 0.475$. The increase in E_c gets progressively larger for higher $\hat{s}$ values.

When a shear stress is imposed ($\rho_{\mathrm{xy}} \neq 0$), the $E_c - \hat{e}$ trends follow those for $\rho_{\mathrm{xy}} = 0$. Over the range of $\hat{e}$, the effect of $\mathcal{L}$ is as follows. At $\mathcal{T} = 0.75$, E_c values at $\mathcal{L} = -1.0$ (Fig. 11a) and $\mathcal{L} = 0$ (Fig. 11b) are lower than their corresponding values for $\rho_{\mathrm{xy}} = 0$ but ρ_{xy} has no effect on E_c for $\mathcal{L} = 0.5$ (Fig. 11c). On the other hand, at $\mathcal{T} = 2.0$ is unaffected by $\mathcal{L}$. Over the range of $\mathcal{L}$, the relative increase in E_c with $\hat{e}$ at $\mathcal{T} = 0.75$ is $\sim 25\%$. On the other hand, at $\mathcal{T} = 2.0$ the relative increase is $\sim 100\%$ over the same range of $\hat{e}$. That is, for a fixed $\hat{s}$ an SH material exhibits an improvement in E_c compared to an RH material and this improvement increases with increasing $\mathcal{T}$. Notably, these relative improvements E_c with $\hat{e}$ are independent of $\mathcal{L}$ and ρ_{xy}.

Fig. 11d-11f shows the corresponding plots of E_f defined earlier. The trends are identical to E_c. At first glance, it appears that there is no perceptible quantitative difference between E_c and E_f. However, the difference becomes clearer in Fig. 12 where we plot the *relative cell ductility* defined as $\hat{E}_{\mathrm{cell}} = (E_f - E_c)/E_c$ versus $\hat{h} = \hat{s}/\hat{e}$. For $\mathcal{T} = 0.75$, and 1.0, $\hat{E}_{\mathrm{cell}}$ is insensitive to $\hat{h}$. At higher $\mathcal{T}$ levels though, $\hat{E}_{\mathrm{cell}}$ shows a non-monotonic trend. As seen, for a given $\mathcal{L}$, $\hat{E}_{\mathrm{cell}}$ is the largest for $\hat{h} \ll 1$ and tends to be the lowest for $\hat{h} \sim 1$ (IH materials). In other words, for IH materials, ultimate failure occurs soon after the coalescence process begins. By way of contrast, for $\hat{h} \ll 1$ (SH materials) or $\hat{h} \gg 1$ (RH materials) ultimate failure can

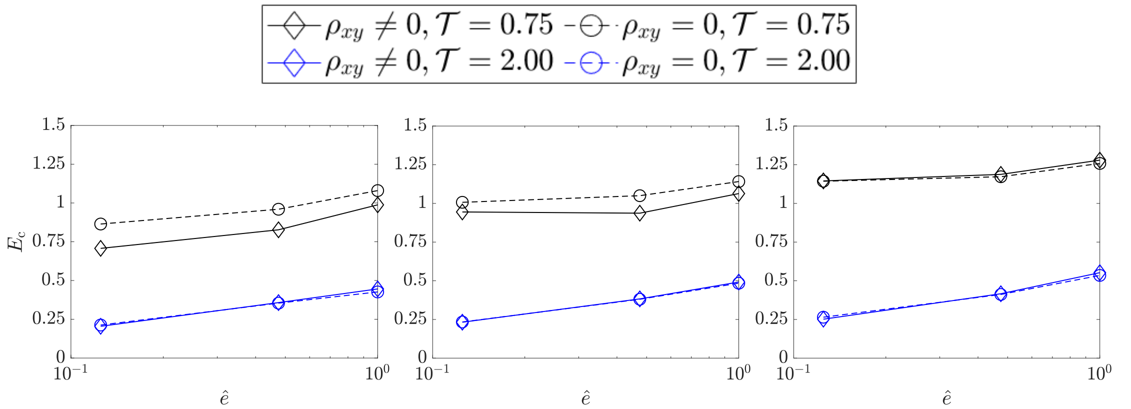

(a) $\mathcal{L} = -1.0$ **(b)** $\mathcal{L} = 0$ **(c)** $\mathcal{L} = +0.5$

(d) $\mathcal{L} = -1.0$ **(e)** $\mathcal{L} = 0$ **(f)** $\mathcal{L} = +0.5$

Fig. 11 Effect of $\hat{e}$ on the (a-c) strain to the onset of coalescence (E_c), (d-f) failure strain (E_f), with $\rho_{xy} \neq 0$ (solid lines) and $\rho_{xy} = 0$ (dashed lines) for $\hat{s} = 0.8$.

be delayed, particularly at high $\mathcal{T}$ levels. This behavior is asymmetric with respect to $\hat{h}$ and the largest gains (for a fixed $\mathcal{L}$) are seen for $\hat{h} \ll 1$. Given that the trends of E_c and E_f are agnostic to ρ_{xy} (at least the shear ratios considered here), the $\hat{E}_{cell}$ trends are also unaffected by ρ_{xy}.

5 Conclusions

In this work, we numerically investigate the void growth and coalescence in plastically isotropic materials exhibiting sigmoidal stress-strain responses. The results extend well beyond those presented in a recent work [8] in two respects - (i) a wider and more realistic range of material hardening characteristics are considered, and (ii) the effect of intermediate principal stress is explored. Several important conclusions are drawn:

1. The cell responses of the three material types (RH, IH, and SH) may be described in terms of two distinct transitions as a function of $\mathcal{T}$. For $\mathcal{T} \leq \mathcal{T}_{low}$, a sigmoidal hardening response is observed, with $E_c \gg E_{peak}$. This is followed by a response characterized by strain hardening, with $E_c \approx E_{peak}$ in the regime $\mathcal{T}_{low} < \mathcal{T} \leq \mathcal{T}_{high}$. Finally at $\mathcal{T} > \mathcal{T}_{high}$, the strain hardening response is replaced by a lack of strain hardening and $E_c \gg E_{peak}$. The occurrence of both transitions (i.e., $\mathcal{T}_{low}$ and $\mathcal{T}_{high}$) is determined by the sigmoidal hardening rate. RH materials only exhibit the first transition, while SH materials lack the first transition at least in the regime of $\mathcal{T}$ considered here. IH materials demonstrate both transitions.
2. In the absence of an imposed shear stress, porosity evolution exhibits stagnation, which coincides with the stagnation in the thinning of lateral ligaments. In RH materials, it is observed over the entire range of $\mathcal{T}$ investigated in this work whereas in IH materials the behavior tends to be tempered at high $\mathcal{T}$ values. SH materials do not show any perceptible stagnation.
3. The broad trends of the stress-strain responses and porosity evolution in the presence of shear stress are similar to those in its absence. With decreasing $\mathcal{L}$, the presence of a shear stress lowers E_c at moderate levels of triaxiality. At high triaxiality levels, SH materials exhibit substantial improvement in E_c relative to RH materials irrespective of whether a shear stress is imposed or not. A much lower improvement is observed at lower triaxiality levels.
4. At high triaxiality levels, the relative cell ductility shows an improvement in the values of the effective material hardening rates that are either smaller or larger than unity. While this does not indicate a

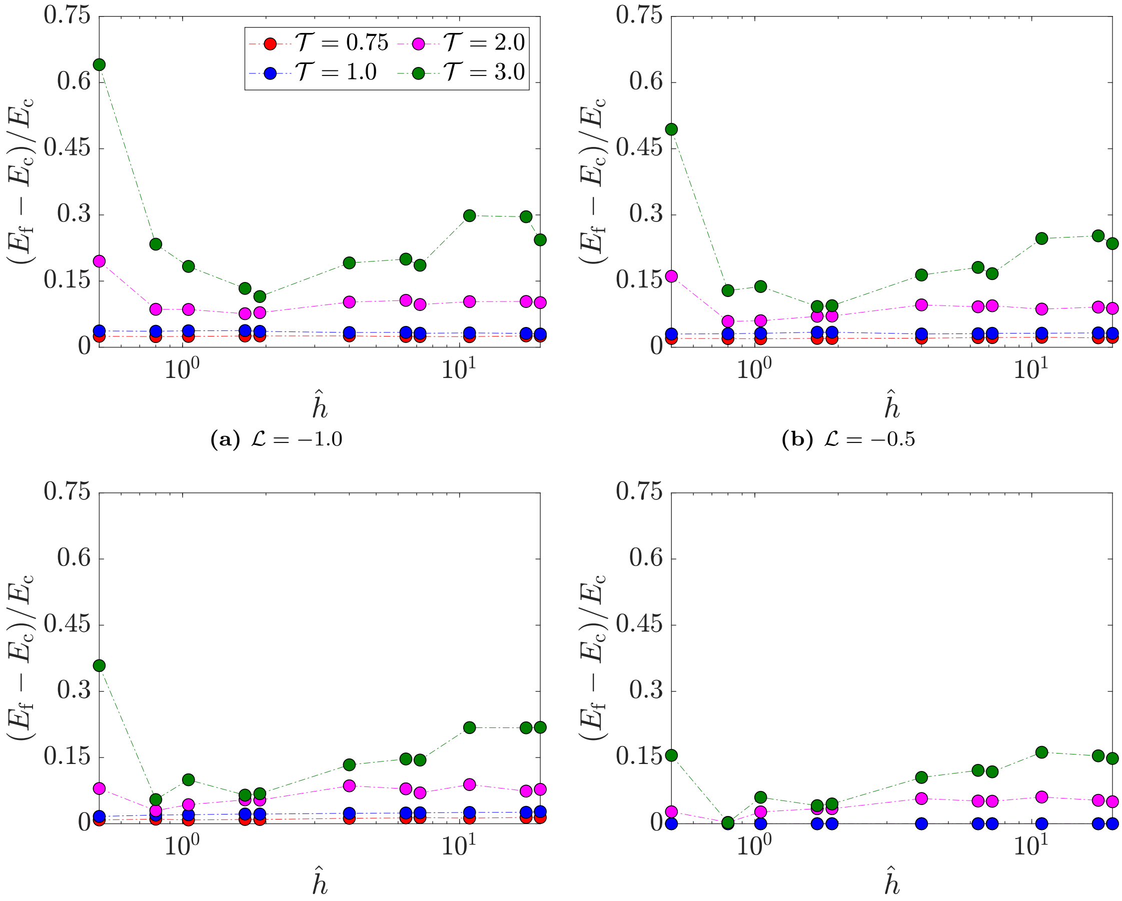

(a) $\mathcal{L} = -1.0$

(b) $\mathcal{L} = -0.5$

(c) $\mathcal{L} = 0.0$

(d) $\mathcal{L} = +0.5$

Fig. 12 Relative cell ductility as a function of the effective material hardening rate ($\hat{h}$) for $\rho_{xy} = 0$.

high overall ductility, it suggests that such materials can sustain non-negligible strains beyond those that correspond to the onset of the coalescence process. The largest improvement in the relative cell ductility is seen for RH materials.

Acknowledgements SD and SPJ acknowledge support provided by the National Science Foundation under Grant Number CMMI-1932976. The authors acknowledge the use of the Opuntia Cluster and the advanced support from the Research Computing Data Core at the University of Houston to carry out the research presented here.

Conflict of interest

The authors declare that they have no conflict of interest.

References

1. J.R. Rice, G. Rosengren, Journal of the Mechanics and Physics of Solids **16**(1), 1 (1968)
2. D.M. Tracey, Engineering Fracture Mechanics **3**(3), 301 (1971)
3. L. Lecarme, C. Tekog, T. Pardoen, et al., International Journal of Plasticity **27**(8), 1203 (2011)
4. E.W. Kelley, W.F. Hosford, (1967)
5. A. Pedicini, R.J. Farris, Polymer **44**(22), 6857 (2003)
6. S. Zhang, Z. Feng, S. Zhang, B. Zhang, W. Liu, N. Zhang, S. Chen, S. Luo, International Journal of Mechanical Sciences **238**, 107862 (2023)
7. P.P. Indurkar, S. Baweja, R. Perez, S.P. Joshi, International Journal of Plasticity **132**, 102762 (2020)
8. P.P. Indurkar, S.P. Joshi, Journal of Applied Mechanics **86**(9) (2019)
9. L.E.B. Dæhli, C. Tekoğlu, D. Morin, T. Børvik, O.S. Hopperstad, Journal of the Mechanics and Physics of Solids **164**, 104873 (2022)
10. Y. Bao, T. Wierzbicki, International Journal of Mechanical Sciences **46**(1), 81 (2004)
11. I. Barsoum, J. Faleskog, International Journal of Solids and Structures **48**(6), 925 (2011)

12. M. Dunand, D. Mohr, Journal of the Mechanics and Physics of Solids **66**, 133 (2014)
13. V. Vishwakarma, S.M. Keralavarma, International Journal of Solids and Structures **166**, 135 (2019)
14. S. Haltom, S. Kyriakides, K. Ravi-Chandar, International Journal of Solids and Structures **50**(10), 1507 (2013)
15. M. Scales, N. Tardif, S. Kyriakides, International Journal of Solids and Structures **97**, 116 (2016)
16. M. Torki, S. Keralavarma, A. Benzerga, Journal of the Mechanics and Physics of Solids **153**, 104468 (2021)
17. C. Tekoglu, International Journal of Solids and Structures **51**(25-26), 4544 (2014)
18. J. Koplik, A. Needleman, International Journal of Solids and Structures **24**(8), 835 (1988)
19. A. Benzerga, Private communication (2023)
20. M.E. Torki, A.A. Benzerga, Extreme mechanics letters **23**, 67 (2018)
21. R. Vigneshwaran, A. Benzerga, in Magnesium Technology 2022 (Springer, 2022), pp. 293–297
22. R. Vigneshwaran, A. Benzerga, Journal of Magnesium and Alloys (2023). DOI https://doi.org/10.1016/j.jma.2023.04.013. URL https://www.sciencedirect.com/science/article/pii/S2213956723000890